Densification behaviour and three-dimensional printing of Y2O3 ceramic powder by selective laser sintering

A. Ratsimba, A. Zerrouki, Nicolas Tessier-Doyen, Benoit Nait-Ali, Damien André, Patrice Duport, A. Neveu, N. Tripathi, F. Francqui, Gaëlle Delaizir

To cite this version:

A. Ratsimba, A. Zerrouki, Nicolas Tessier-Doyen, Benoit Nait-Ali, Damien André, et al.. Densification behaviour and three-dimensional printing of Y2O3 ceramic powder by selective laser sintering. Ceramics International, 2021, 47 (6), pp.7465-7474. 10.1016/j.ceramint.2020.11.087 . hal-03281678

HAL Id: hal-03281678
https://unilim.hal.science/hal-03281678v1

Submitted on 10 Mar 2023

Version of Record: https://www.sciencedirect.com/science/article/pii/S0272884220334039
Manuscript_9f8758036fca9f16993da7fca727ea4b

Densification behaviour and three-dimensional printing of Y_2O_3 ceramic powder by selective laser sintering

A. Ratsimba[1], A. Zerrouki[1], N. Tessier-Doyen[2], B. Nait-Ali[1,2], D. André[1,2], P. Duport[1,2], A. Neveu[3], N. Tripathi[3], F. Francqui[3], G. Delaizir[1,2*]

[1]ENSIL-ENSCI, Centre Européen de la Céramique, 12 rue Atlantis, 87068 Limoges, France

[2] Institut de Recherche sur les Céramiques, UMR CNRS 7315, Centre Européen de la Céramique, 12 rue Atlantis, 87068 Limoges, France

[3]Granutools, Rue Jean-Lambert Defrêne 107, 4340 Awans, Belgium

Abstract

The selective laser sintering (SLS) of an yttria (Y_2O_3) ceramic powder was studied to understand both the effects of i) the initial yttria particle characteristics on the powder bed behaviour and ii) the process conditions (laser power, scanning speed, hatching space) on the sintering/melting of three-dimensionally printed objects. The roughness of the powder bed, a sensitive indicator of the layer bed quality, was determined through three-dimensional optical profilometry and the powder bed packing density was modelled using the discrete-element method. Complex shaped objects including spheres and open rings were successfully fabricated by the SLS three-dimensional printing. In addition, SLS cube-shaped samples were characterized by X-ray diffraction and scanning electron microscopy. The open pore volume fraction significantly decreased from 41% without a post-SLS heat treatment to 31% with a post-SLS heat treatment at 1750 °C for 20 h under secondary vacuum. Finally, an anisotropy in elastic properties has been highlighted, Young's modulus reaches 11 GPa in the stiffest direction.

Keywords: selective laser sintering, yttria, powder bed fusion

*Corresponding author: gaelle.delaizir@unilim.fr

1. Introduction

Yttria (Y_2O_3) is a promising material for a wide range of uses. It has outstanding physical, mechanical and chemical properties, an infrared transparency up to 8 μm, a high thermal conductivity, refractoriness, both high fracture toughness and hardness, and a high corrosion resistance, suitable for various applications such as infrared windows and domes, cutting tools or corrosion resistant containers [1–7]. Under ambient conditions, yttria exhibits an isotropic cubic structure. Yttria ceramic materials are usually fabricated by the sintering of powders using conventional (natural sintering, hot uniaxial pressing, hot isostatic pressing) and non-conventional (spark plasma sintering) techniques [8, 9]. Vacuum as the sintering atmosphere, nanopowders and/or sintering agents (LiF, ZrO_2, or La_2O_3) have been used to reduce the final porosity and retain the transparency [10–17].

The emerging additive technologies (three-dimensional (3D) printing), including stereolithography, inkjet printing, robocasting, binder jetting, and selective laser sintering (SLS), enable to obtain objects with complex shapes. The main advantage of the SLS over the other techniques is the absence of debinding step. The SLS, a layer-by-layer additive technology, comprises two critical steps: i) powder bed and ii) lasering steps, which are repeated until the object, previously defined by a Computer-Aided Design model, is fabricated.

This technique is advanced for some materials such as metals and polymers [18–20]. The boundary between sintering and melting in this technology is subtle and depends on the local laser energy density. In this regard, the term SLS is also associated to the term selective laser melting (SLM) or powder bed fusion. The latter mechanism occurs in the sintering of metals and polymers. The SLS technology for ceramic powders is less developed owing to their intrinsic physical and chemical properties (e.g., refractoriness), but has attracted interest among the research and industrial communities because of its potentials for aeronautic, biomedical, and metallurgy applications [21]. In 1998, Klocke *et al.* reported the first ceramic powder fabricated by the SLS on a zirconium silicate material [22]. Subsequently, studies have been carried out on ceramic powders (alumina and glass) in Limoges, France, which led to the development of Phenix System company in 1999 (now 3D Systems) [23]. Since 1998, various studies have been carried out on alumina, porcelain, composites, nitrides, carbides, and yttria-stabilized zirconia based ceramic powders using the SLS technique [24–36]. The SLS can be direct (dSLS) or indirect (iSLS). In the dSLS, only the laser energy is used to locally consolidate the powder, while in the iSLS, a sintering agent or low-melting-point material, such as glass or polymer, is used to improve the densification of the final object. Using this technique and ball-milled mixtures of alumina and stearic acid, Liu *et al.* manufactured ceramic bars with densities up to 88% [36]. The raw materials used in the SLS technique can be powders or slurries, which provide better results regarding the packing density [37, 38]. Therefore, the combined use of a slurry and iSLS could be the best approach to achieve a high densification of the final object. For example, alumina ceramic parts with densities up to 98% were produced by iSLS starting from a slurry composed of an alumina powder coated with polyvinyl alcohol [37]. **If the main drawback of the SLS technique of ceramic powder remains the residual porosity that is difficult to eliminate, in some cases, this porosity is expected and well controlled to elaborate ceramic foams in order to be used as filters or thermal insulator. The unconventional SLS technique is a powerful method that allows getting complex ceramic foam structures with controlled pore size distribution [39, 40].**

In this study, we investigate the densification behaviour and microstructure of a microcrystalline Y_2O_3 powder without sintering aids using the dSLS technique. A careful preliminary characterization of the powder packing ability has been performed with an automated tapped density meter allowing user-independent accurate measurements of the bulk and packed density as well as the whole packing dynamics. Moreover, flowability and ability of the powder to charge due to triboelectric effects have been quantified. A dynamic discrete-element method (DEM) simulation mimicking the layering of powder in SLS process was carried out to understand the influence of platelet morphology on the particle packing. The influence of post-SLS heat treatments under different atmospheres (air and vacuum) on the open pore volume fraction and elastic properties of the final objects is also investigated.

2. Experimental methods

A commercial yttrium oxide powder (99.99%, US Research Nanomaterials, Inc.) was used as starting powder. **No sintering agents or dopants were added to the yttria powder in the following SLS experiments.**

2.1 SLS and post-processing

Yttria objects were designed and 3D-printed using a PM100T (Phenix Systems, **Riom, France**) SLS apparatus equipped with a Nd^{3+}-doped fiber laser (1.06 µm, 200 W), a x–y scanner and a Ø 100 mm circular sintering plateau. The apparatus consisted of a powder alimentation container, a roller and a sintering platform (homemade porcelain plateau). The roller has a rotation speed of 0.42 rad.s^{-1} with a translation speed fixed at 40 mm.s^{-1}.The layer thickness was fixed to 60 µm. As explained in [30], we estimate the beam diameter by optical microscopy from the laser trace to be approximately equal to 70 µm using a porcelain plateau coated with a graphite spray. Various scanning strategies can be applied during the laser sintering: stripe hatch with either a continuous wiring mode or pulse mode, meander hatch, chess-board hatch, etc. [41]. In this study, we used a strip hatch with unidirectional vectors and difference of 90° between even- and odd-layer vectors. All experiments were carried out at a laser scanning velocity of 0.5 m·s^{-1}. We varied the distance between the laser vectors (or hatching space) in the range of 10 to 70 µm and laser power in the range of 30 to 85 W. The laser-sintered objects were heat-treated at 1600 or 1750 °C for 2 h under air, and at 1750 °C for 20 h under secondary vacuum (ECM Lilliput furnace, **Grenoble, France**, 10^{-6} mbar) to decrease open porosity of the final objects.

2.2 Characterizations

2.2.1 Powder characterizations

The particle size distribution of the yttria powder was determined using a Malvern Mastersizer **2000** apparatus **(Worcestershire, UK).** The specific surface area was measured according to the Brunauer–Emmett–Teller (BET) method using a Micromeritics Tristar equipment **(Norcross, USA)**.

The morphology and particle size of the initial powder and microstructures of the laser-sintered samples were observed using scanning electron microscopy (SEM, JEOL IT 300 LV, **Tokyo, Japan**). Reflectivity measurements of the yttria powder at the laser wavelength (1.06 µm) were performed using an ultraviolet–visible–infrared Lambda 365 Perkin Elmer instrument **(Waltham, USA)** equipped with an integrating sphere.

a) Powder flow measurement method

The experimental setup used to perform the flowability measurement is the GranuDrum from the GranuTools company **(Awans, Belgium)**. This measurement method has been presented in detail in a previous paper [42]. The measurement cell is a horizontal aluminum cylinder of diameter D = 84 mm and length L = 20 mm with glass side walls. The drum is half-filled with the powder. The cylinder rotates around its axis at an angular velocity Ω producing the flow of the grains. A sequence of increasing angular velocities is explored in order to study the rheological behaviour of the powder. For each angular velocity, 40 images of the rotating powder bed separated by 1 s are recorded with a CCD camera. The position of the air/powder interface is extracted by the use of an image processing algorithm. For each rotating speed, the temporal fluctuations of the average position of the interface are computed. A dynamic parameter, called the cohesive index σ_f, is computed from these fluctuations and is directly related to the cohesive interactions between the particles. Furthermore, after the increasing velocity sequence, a reverse (decreasing) velocity sequence is performed to highlight a possible thixotropic behaviour.

b) Powder tribocharging

GranuCharge from GranuTools **(Awans, Belgium)** is a recently developed triboelectric charger used to measure the total electrostatic charge created inside a granular medium during a flow in contact with a selected material [43]. The sample is poured by a vibrating feeder in a V-tube and flows to a Faraday cup. The V-tube is an assembly of two tubes of length L=350mm and internal diameter D=47mm to form a V shape with an angle of 90°. For the present study, 316 L stainless steel has been selected. The Faraday cup is connected to a dedicated electrometer able to measure electrostatic charges. At the end of the flow, the total value of the electric charge Q present in the powder is measured and the charge density q=Q/m, where m is the sample mass, is computed.

c) Packing density

The automated tapped density measurement device GranuPack from GranuTools [42, 44] **(Awans, Belgium)** has been used. The measurement is done in a metallic tube to avoid the accumulation of electric charges during the measurement. The diameter and the length of the tube used to perform the studies presented in this paper are D = 26 mm and L = 100 mm. In order to obtain a reproducible and spatially homogeneous initial packing, the following initialization protocol is used.

A narrower and bottomless tube is inserted into the measurement tube. Afterward, the initialization tube is filled with the granular material and is removed upward at a low and constant velocity v = 1 mm/s leaving the grains to rearrange themselves in the measurement tube. Then a light hollow cylinder is gently placed on the top of the pile to keep it flat during the compaction process. To apply a tap on the packing, the tube goes up to a height of $\Delta z = 1$ mm and experiences a free fall over the same height. After each tap, a distance sensor measures the position of the hollow cylinder. From this distance, the height h and the volume V of the pile are computed. As the introduced mass of powder is known, the bulk density evolution as a function of the tap number is calculated.

The bulk density is the ratio between the mass m and the volume V of the powder.

d) Surface topography of powder bed

The surface topography of the yttria layers before the laser sintering was determined using a profilometric microscope (ZoomSurf, Fogale Nanotech®, **Nimes,** France) based on the measurement of interference fringes. The 3D surface topography was then numerically obtained using the Mountains Map® software. As this technique did not involve contact with the investigated surface, the powder bed was not disturbed. Before the lasering step, the quality of the deposited layer related to the organization of ceramic powder particles could be estimated through the average roughness (S_a).

e) Simulation

In addition to these characterizations, discrete-element method (DEM) simulations were carried out to model the powder bed and its packing density.

2.2.2 3D sample characterizations

The open porosity (ν_{op}) of the different yttria objects was measured using a homemade Archimedes apparatus under water and vacuum using [45]

$$\nu_{op} = \frac{m_3 - m_1}{m_3 - m_2}, \qquad \text{(eq. 1)}$$

where m_1, m_2, and m_3 are the masses of the dry sample, water-impregnated sample measured in water, and water-impregnated sample measured in air, respectively.

The structures of the initial powder and 3D SLS objects obtained with and without the post-processing (heat-treatment) were evaluated by X-ray diffraction (XRD, Bruker D8 Advance, **Billerica, USA**).

Elastic properties of cube-shaped samples have been estimated using pulse echography technique: measurements in infinite medium mode operating in transmission have been performed at a frequency of 600 kHz. Tensile-compressive and shear acoustic waves are sent through the thickness of samples using two pairs of transducers to evaluate both longitudinal and transversal wave propagation velocity values. The knowledge of the apparent density is also required to determine the values of Young's modulus in the 3 directions of the specimens.

3. Results and discussion

3.1 Powder characterizations and powder bed

The SEM images in Figure 1 show that the commercial yttria powder exhibits platelet and sheet structures. The particle size distribution of the commercial yttria powder (presented in Figure 2) is nearly unimodal with a median diameter D_{50} of approximately 5 µm. Main physical characteristics including density, structure, reflectivity at the laser wavelength (1.06 µm), and particle diameter are reported in Table 1.

3.1.1 Packing properties

Several studies highlighted the importance of the shape and particle size distribution of the powder bed for the optimization of the packing density [45–49]. An improved packing density may provide a better layer packing during the SLS, which is favorable to achieve improved qualities and densities of the final objects. The shapes (almost spherical, spheroidal, platelet, dendritic, irregular, angular, etc.) of the particles also determine the behaviour of the powder even for similar sizes. Dupont *et al.* studied the influence of the yttria powder morphology on the green density through a thermodynamic model [49]. They reported that the maximum packing density was achieved for small and thick regular or irregular platelets. The latter form is analyzed in this study. Packing properties of the yttria powder has been evaluated with the GranuPack. The Hausner ratio, a measure of the compressibility of the powder, is computed as the ratio of the density after 500 taps to the initial apparent density. The measured bulk density was 0.85 g/cm^{-3} and the tapped density was 1.26 g/cm^{-3}, leading to a Hausner ratio of 1.49. This high value of the Hausner ratio indicates of a very poor flowability [50]. Indeed, a cohesive powder is able to sustain a loose packing and so a low apparent density compared to the packed one.

Considering a given particle shape, fine particles exhibit a higher packing density than that of coarse particles. A multimodal particle size distribution could be beneficial to fill the voids and optimize the packing density of the powder bed [46]. D_{100} of the powder particle size distribution should be lower than the thickness of the powder layer, in our case smaller than 60 µm. The measured D_{100} was approximately 20 µm, according to Figure 2.

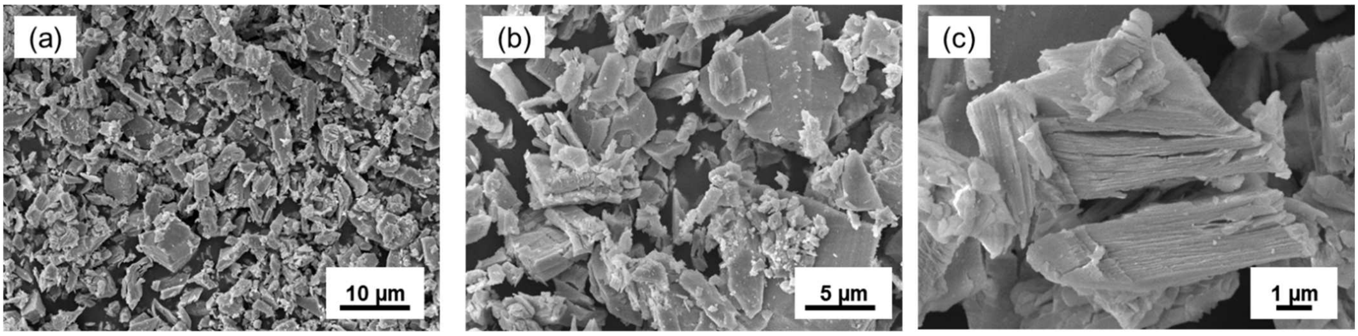

Figure 1. *SEM images of the commercial Y_2O_3 powder at different magnifications.*

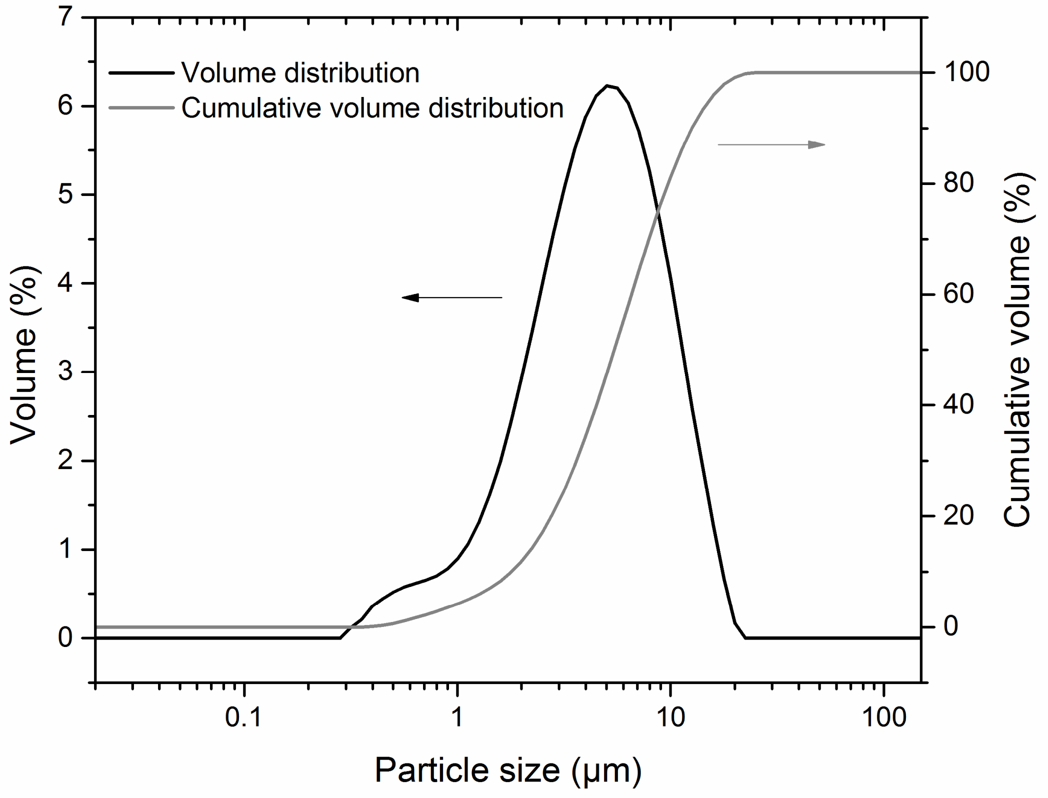

Figure 2. *Particle size distribution of the Y_2O_3 commercial powder.*

Table 1. *Physical properties of the yttria powder.*

Compound	**Melting temperature**	**Density**	**Reflectivity (at 1.06 µm)**	**Particle size distribution**			**BET specific surface area**	**Crystalline structure**
				D_{10}	D_{50}	D_{90}		

Y_2O_3	2400 °C	4.83	90%	1.8 µm	5.4 µm	12.6 µm	3.8 $m^2 \cdot g^{-1}$	Cubic

Figure 3 shows the topography of the yttria powder bed. The simple roughness measurement is reliable for the detection of possible defects such as voids in the arrangement of the powder particle compacts. The experiment was performed on 60 layers without laser sintering between two powder layers. The average S_a measured for 12 areas of the plateau was ~ 5.4 ± 0.3 µm. The amplitude along the plateau was in the range of 4.6 to 5.7 µm, which is satisfactory. In order to highlight a strong and homogeneous particle packing, this value must be as low as possible with a low standard deviation (scattering): indeed, defects such as lack of powder and disturbance in the arrangement of powder particles in a given layer can significantly reduce the quality of the final 3D object.

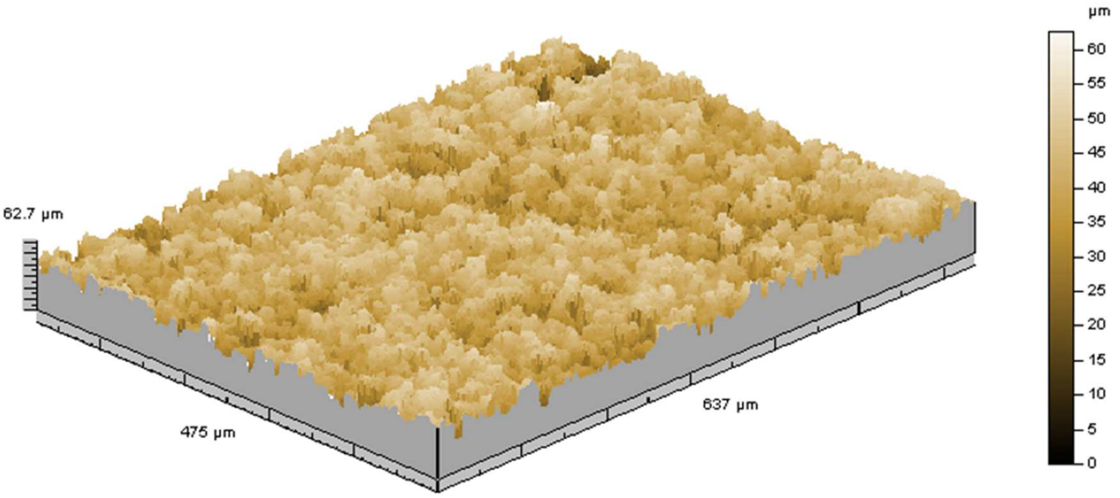

Figure 3. *3D topography profile of the Y_2O_3 commercial powder bed.*

For the determination of the packing density, the apparent density of 60 powder layers was determined by measuring the height of the layers, diameter of the plateau, and weight of the powder (geometric density). The roughly estimated powder bed packing density was 37 ± 5% (1.79 g/cm^3). This value is higher than the one obtained by the tapped density measurements performed with the GranuPack equipment (26.1%, 1.26 g/cm^3). The stress applied to the powder bed by the roller recoater thus helps to increase the layer packing density.

3.1.2 Powder flowability

Powder rheological behaviour has been investigated with the GranuDrum. The Cohesive Index versus the drum rotating speed is presented in Figure 4. The yttria powder exhibits a cohesive behaviour, leading to a cohesive index above 50 for the range of speeds investigated. A high cohesiveness leads to a decrease of spreadability and thus the appearance of irregularities on the powder bed. The satisfactory layer homogeneity observed in the SLS printer for the yttria powder (3D topography profile, see Figure 3) may thus be attributed to the performance of the roller recoater and the peculiar platelets particle shape. Moreover, a slight shear-thinning behaviour *i.e.* a decrease of cohesiveness with increasing applied stress is observed at low speeds. According to these results, the yttria powder is expected to have a better process ability at higher shear rates. Different effects can be at the origin of this shear-thinning. In the case of granulation due to agglomeration of fine particles into larger ones, the increase of the mean particle size is accompanied with a decrease of cohesiveness. However, the thixotropic behaviour which is usually a signature of agglomeration has not been observed here, and the formation of agglomerates has not been visually observed. Another explanation may be a higher distance between the particles due to the aeration of the powder that leads to a decrease of the cohesive interaction intensity, and thus a decrease of the global cohesiveness. Furthermore, the platelet shape may favor the alignment of the particles and the formation of layers that could lead to an increase of flowability.

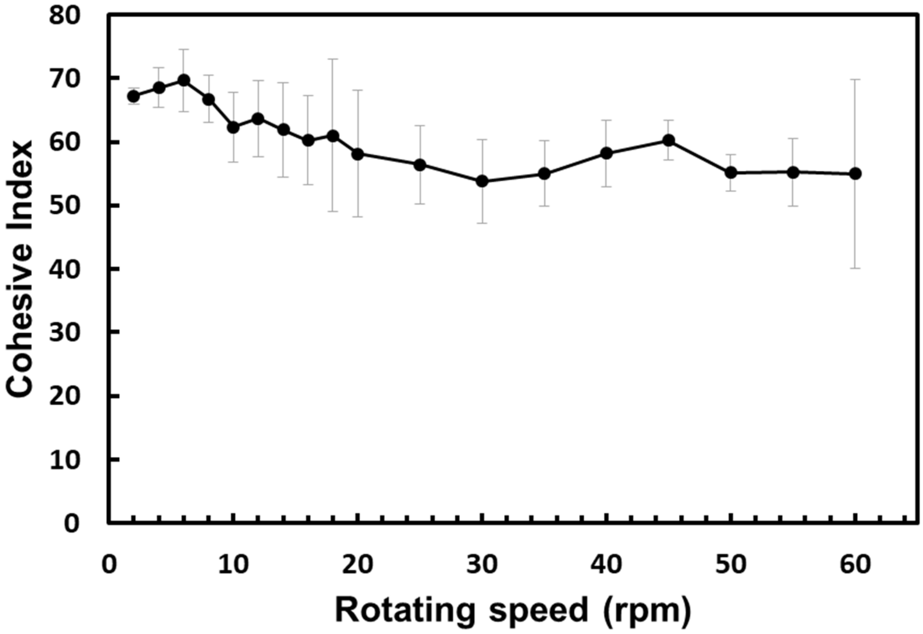

Figure 4. *Cohesive index versus the drum rotating speed obtained with the GranuDrum for increasing speeds sequence. Error bars are standard deviation estimated from three measurements.*

3.1.3 Electrostatic charge buildup

Electrostatic charge buildup has been investigated with the GranuCharge. Indeed, the charges that arise from the contact between particles and the contact with recoater cylinder can lead to an increase of the global cohesiveness of the powder. The yttria powder exhibits a very low initial charge of -0.01 nC/g, and a low charge buildup due to the flow through the pipes Δq=-0.20 nC/g. These results indicate that the powder is only fewly influenced by tribocharging due to contact with stainless steel. However, powder sticking on the recoater cylinder has been observed during recoating operations inside the printer, but this phenomenon disappears when the powder is heated in an oven at 110°C for 24h prior to SLS experiments. The very low sensibility of the yttria powder to tribocharging allows thus to attribute this sticking to capillary bridges formation between particles and recoater cylinder rather than electrostatic interactions.

3.2 Simulation of the powder bed packing density

Discrete-element method (DEM) simulations were carried out to understand the influence of the yttria particle shape and particle size distribution on the powder layer development and its packing density. The commercial yttria powder was composed of irregular platelets with sizes in the range of 200 nm to 20 µm (Figures 1 and 2). Since the intial study by Cundall and Strack in 1979 [51], the DEM has been extensively used for modelling the dynamic behaviours of granular media such as ceramic powder. The aim of this method, also referred as “distinct-element method”, is to solve a class of problems that cannot be treated by continuous or analytical approaches such as packing problems and hourglass flows of granular media. In the DEM, a particle is modeled through discrete elements able to move in the 3D space. The particle movements are individually driven by the Newton’s second law. The external forces and torques are coming from mechanical contacts where the particles interact. Depending on the properties of the granular material, the contacts can be contacts with and without friction, repulsive, adhesive, linear, nonlinear, etc. In this study, the chosen contacts were repulsive with static and dynamic friction coefficients equal to 0.3 that correspond to a common friction coefficient value.

For these simulations, the free GranOO DEM software was chosen because it allows to use spherical and non-spherical discrete elements. Contact detection with non-spherical elements is not straightforward. GranOO software is based on i) the Gilbert–Johnson–Keerthi expanding polytope algorithm [52] for the narrow-phase contact detection and ii) axis-aligned bounding box tree algorithm [53] for the broad-phase contact detection.

The aim of these numerical simulations was to study the influence of the platelet shape on the packing density. In the preliminary step of the simulation, a given space was filled with discrete elements according to the particle size distribution (Figure 2). As shown in Figure 5a, "particle rain" simulations were carried out to fill a given bounding box. In these "rain simulations", the grains appear randomly at a given altitude and fall down owing to the gravity (see Figure 5a). The box exhibits dimensions of 1 × 2 × 0.2 mm and contains approximately 12 000 particles.

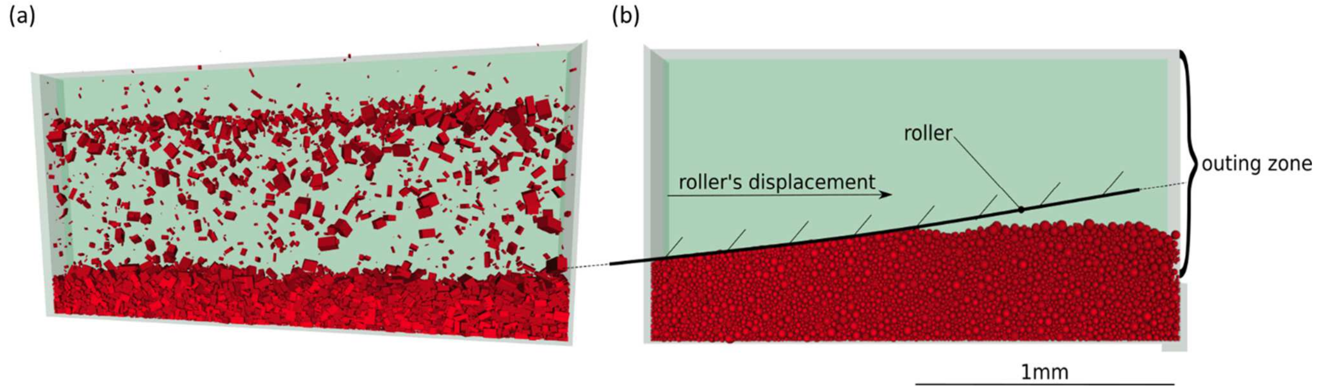

***Figure 5.** (a) Particle rain simulation. (b) Simulation of the layering process.*

The final configurations of the "rain simulations" were used as initial configurations of a second step simulations In these second steps, as shown is Figure 5b, the layering or powder bed simulations was simulated To simulate the layering, a cylindrical roller exhibiting a diameter of 4 cm was introduced in the simulation. The roller moved with a horizontal displacement at a constant velocity. The initial configuration is shown in Figure 5b and in the video. The zone referred as "outing zone" in Figure 5b is the zone where the discrete elements could freely fall down and are removed from the simulations. The simulation was completed when the roller translated a maximum distance of 8 mm. This length ensured that the roller carried out a full pass on the 2-mm bounding box.

test.mp4

This simulation, which mimicked the layering, was performed for platelet particles, but could be also carried out with other shapes such as spheroids, needles, etc. The local volume fraction was computed before and after the roller pass. The volume fraction or packing density reached 57% for the platelet shape. The orientations of the particles along their maximum lengths were naturally favored by the mechanical action of the roller during its motion. Therefore, a more organized granular arrangement and lower pore volume fraction of the particle packing were obtained. The tapped density was 42.8 ± 0,5%, while the model value was 57%. This difference can be explained by the morphology of the particles considered in the model, which could not be easily simulated and was not perfectly similar to real particles.

The DEM was used to qualitatively evaluate the influence of the particle shape. The presented results are useful for a better understanding of the layering process. The platelet shapes combined with the roller displacement promoted the granular packing of the powder in the preferred direction. More accurate simulations can be performed in further studies to understand the key step of the SLS and to optimize the roller movement, particle shape, and grain size distribution.

3.3 Shaping of laser-sintered 3D objects

To locally consolidate the powder, various parameters were evaluated including the laser power and hatching space. The experimental results are summarized in Figure 6. The total energy supplied to consolidate the layer increased with the movement to the right and bottom parts. The laser energy density (*E*) was calculated by

$$E\ (\mathrm{J/cm^2}) = \frac{P}{D \times V}, \quad \text{(eq. 2)}$$

where P is the laser power, D is the laser beam diameter (~70 µm), and V is the laser scanning speed (0.5 $\mathrm{m \cdot s^{-1}}$). Note that some authors mention equations that include the hatching space to calculate the laser energy density [54].

High energy densities and small hatching spaces lead to molten objects while low energy densities whereas large hatching spaces lead to unconsolidated objects. Therefore, only a set of specific parameters provided consolidated objects, as shown by the green area in Figure 6. We arbitrarily employed the following set of SLS parameters in the green area to obtain the 3D objects: laser power of 63 W, hatching space of 50 µm, speed of 0.5 m·s^{-1}, energy density of 180 J.cm^{-2}, and thickness of the layer of 60 µm.

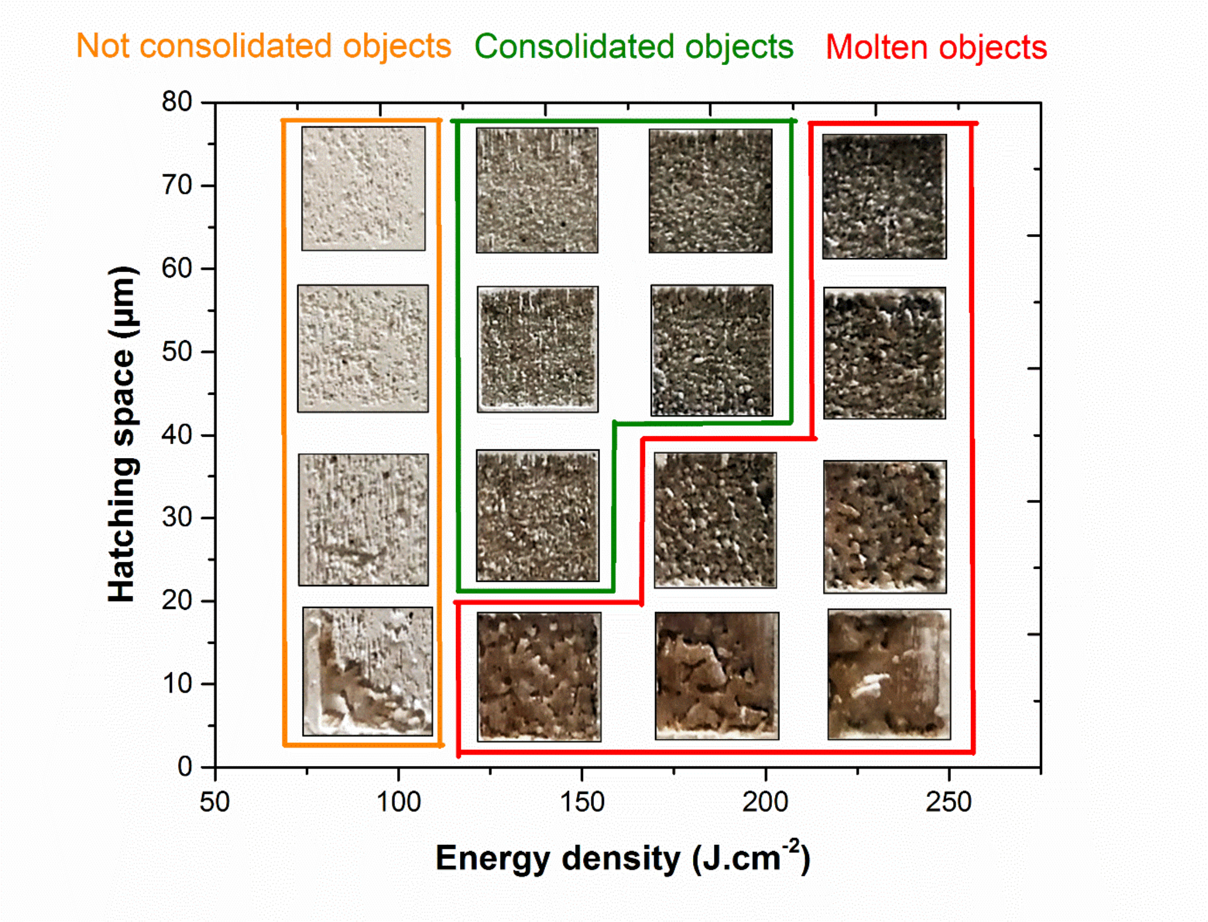

Figure 6. *Experimental diagram for the SLS. The color lines separate the samples with acceptable mechanical handling performances from the unconsolidated samples and objects exhibiting significant deformations due to melting.*

Based on this set of parameters, several objects with complex shapes, including spheres, cubes, and open rings, were fabricated, as shown in Figure 7. The SLS objects exhibited different colors, from light grey (without post-SLS heat treatment) to white and black (post-SLS heat treatments under air and secondary vacuum at 1750 °C, respectively). The latter treatment, which leads to the well-known reduction of oxides, produced black samples owing to the large number of oxygen vacancies [9, 55]. Notably, these samples became white again after an annealing treatment under air at a high temperature for few hours.

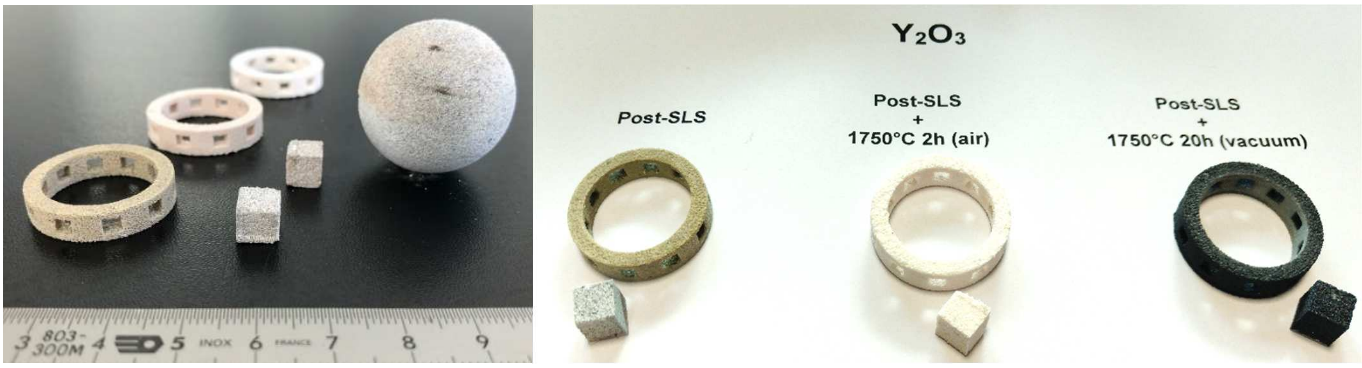

Figure 7. *Photographs of* Y_2O_3 *SLS objects with complex shapes obtained with and without post-SLS heat treatments under air and vacuum.*

3.4 Evolution of phases, pore volume fraction and elastic properties of final SLS objects

XRD patterns of the commercial powder and SLS objects obtained with and without post-SLS heat treatments are presented in Figure 8. The commercial powder and SLS objects obtained with and without a post-heat-treatment at 1650 °C for 2 h under air exhibited a cubic structure (Joint Committee on Powder Diffraction Standards (JCPDS) 19-6322). Additional low-intensity peaks were observed in the pattern of the SLS object obtained with a post-heat-treatment at 1750 °C for 20 h under vacuum. These peaks could be attributed to the non-stoichiometric Y_2O_{3-x} phase [56]. However, the pattern of the same powder subjected to a second heat treatment under air at 1100 °C exhibited the same peaks (Figure 8). The peaks could correspond to the Y_2O_3 hexagonal phase (JCPDS 20-1412). This was not expected, as this phase appears at a high temperature (>2400 °C) under air or at a high pressure [57]. However, as shown in Figure 6, the temperature may have locally exceeded the melting point in the consolidated samples.

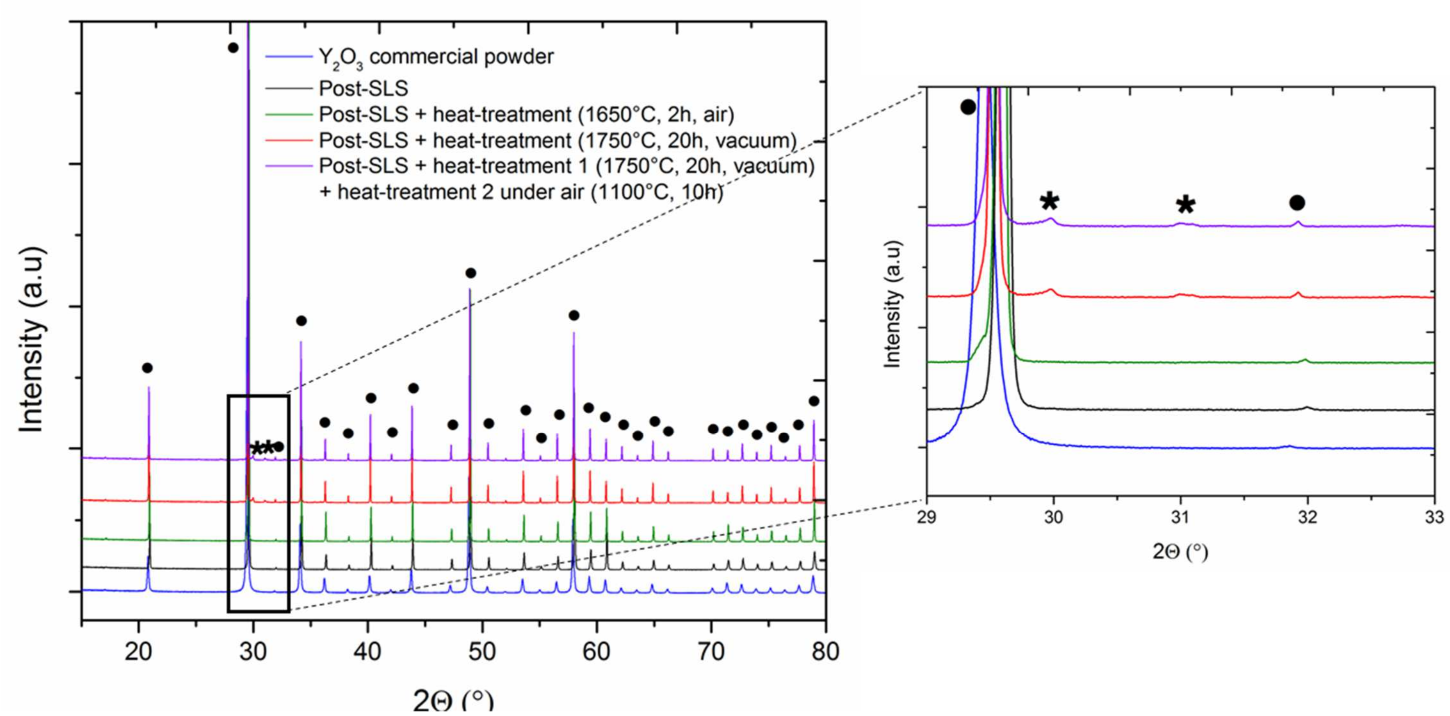

Figure 8. *Powder XRD patterns of the Y_2O_3 SLS objects obtained with and without post-SLS heat treatments (● Y_2O_3 cubic phase (JCPDS 19-6322), ✱ Y_2O_3 hexagonal phase (JCPDS 20-1412)).*

The microstructure of the SLS objects obtained with and without post heat-treatments (under air and vacuum) was observed by SEM. All objects exhibited both open and closed porosity (Figure 9). The open pores had irregular shapes and were rather large. They originated mainly from the voids formed by the particles in the powder bed, which could not achieve a dense assembly, as shown by the measured geometric packing density of the powder bed (37%) or the tapped density.

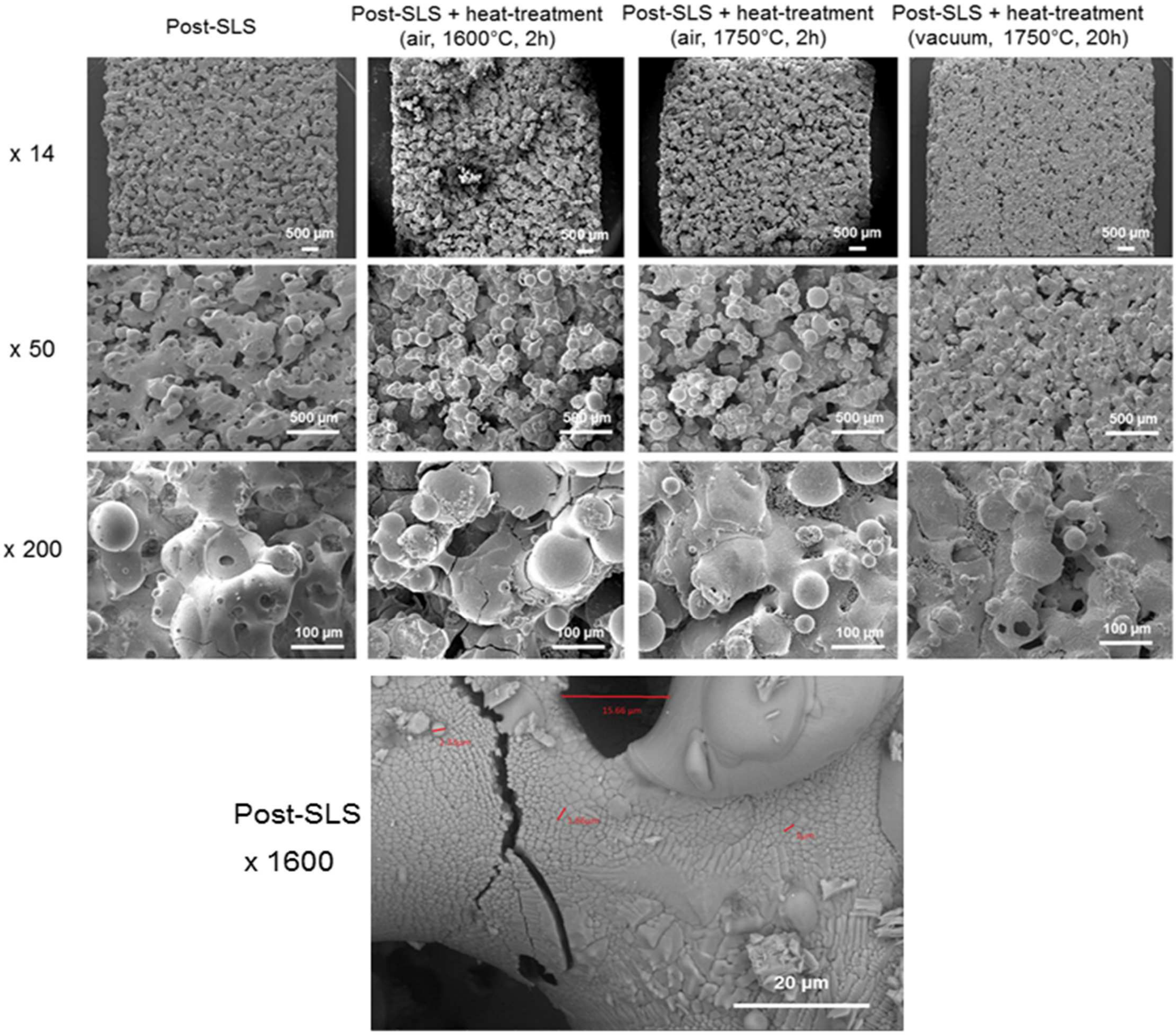

Figure 9. *SEM images (at low and high magnifications) of the post-SLS objects, post-SLS objects obtained with post-SLS heat treatments at 1650 and 1750 °C for 2 h under air, and post-SLS objects obtained with the post-treatment at 1750 °C for 20 h under secondary vacuum.*

The pores also likely originated from the lack of cohesion between two consecutive layers. In this experiment, the energy density was probably insufficient to weld consecutive layers. Notably, slight laser traces and “free” powder could not be observed on the surfaces of the different SLS objects, which implies sometimes an overlap of the laser scans during the SLS. The morphologies of the different objects included coarse agglomerates (~500 µm) of molten particles also known as balling effect due to the poor wetting behaviour of the liquid phase, which evidences locally the very high temperature of the matter irradiated by the laser beam [21]. It is well known that not all released laser energy is used to sinter/melt the yttria powder owing to the different mechanisms of the interaction between the light and material (reflection, diffusion, absorption, etc.). The reflectivity measurement indicates that 90% of the incident light was reflected by the yttria powder (Table 1). Consequently, only a part of the remaining 10% of the incident energy was absorbed to consolidate the powder. Doping of the powder, commonly by carbon, has been carried out to increase the absorption at the laser wavelength [30]. Reflectivity tests were performed to evaluate the influence of the carbon addition to the yttria powder (Table 2). The reflectivity decreased from 90% (0 wt% of carbon) to 50.9% (0.5 wt% of carbon). Even a carbon content of 0.05% was efficient to significantly decrease the reflectivity.

Table 2. *Influence of the carbon addition on the reflectivity of the yttria powder at 1.06 µm.*

Carbon content (wt%)	**Reflectivity at 1.06 µm (%)**
0	90
0.05	66.8
0.1	65.3
0.3	58.5
0.5	50.9

The open porosity of the laser-sintered body was ~ 41 ± 2%, measured with the homemade Archimedes apparatus. For comparison, those of dSLS porcelain and iSLS alumina objects were 47 ± 2% and 45 ± 2%, respectively [20, 26]. The post-SLS treatments at 1650 and 1750 °C under air led to similar values (~39%), while that at 1750 °C for 20 h under secondary vacuum efficiently reduced the open porosity (~31%). The microstructure of the object obtained with the post-SLS heat treatment under vacuum was different from those of the post-SLS objects. The agglomerates of molten particles observed in the post-SLS objects seemed to sinter during the post-treatment under vacuum at the high temperature. However, the diffusion during the post-SLS heat treatment under vacuum at 1750 °C was not sufficient to close the overall open porosity as the pores were initially very large. Therefore, the open porosity was still high. Notably, the high-magnification (1600×) image of the post-SLS object shows some small yttria grains (~1 µm) in some consolidated parts, which demonstrates the fast melting–recrystallization during the SLS.

Young's modulus of SLS yttria cubes has been evaluated by pulse echography technique [58] in 3 directions according to the schematic presented in Figure 10. Note that direction 3 is perpendicular to the layer, and directions 1 and 2 are in the plane of the layers.

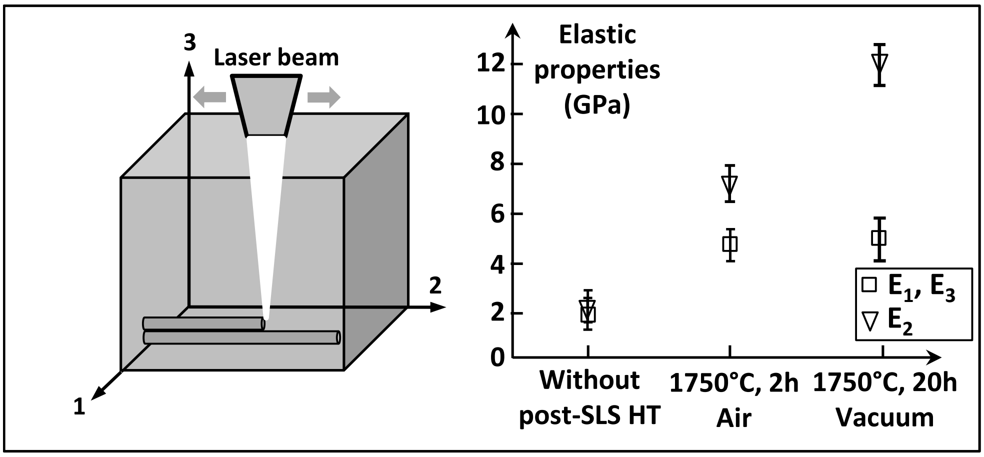

Figure 10. *Young's modulus measurements by pulse echography technique in 3 directions for post-SLS objects without any heat treatment, post-SLS objects obtained with post-SLS heat*

treatments at 1750 °C for 2 h under air and post-SLS objects obtained with the post-treatment at 1750 °C for 20 h under secondary vacuum.

For SLS-samples without any heat treatment, Young's modulus is very low (around 2 GPa) with a high pore volume fraction (around 41%) whatever the direction of measurement. After heat treatment at 1750°C in air, the Young's modulus is multiplied by 2.5 in directions 1 and 3 and by 3.5 in direction 2. If samples are treated at 1750°C during 20h under vacuum, direction 2 exhibits a significant increase in Young's modulus (the value reaches approximately 12 GPa) highlighting an anisotropy in elastic properties. This result can be attributed to a preferential sintering direction of the powder particles under these post heat treatment conditions favored during the SLS processing. However, these measured elastic properties remain rather low compared to pure and fully dense Y_2O_3 materials (≈ 180 GPa for Young's modulus [59]) which is both due to high pore volume fraction and possible less densified local areas in the solid skeleton during SLS processing which may weaken the overall rigidity of samples.

4. Conclusion

Yttria ceramic objects with complex shapes including spheres were fabricated by the dSLS. The size distribution and morphology of the particles influenced the powder packing ability and thus the powder bed packing density, both were estimated experimentally and modelled using the DEM. Also, powder exhibited a shear-thinning behaviour with an increase of flowability with increasing applied shear rate. The roughness of the powder bed was measured optically. Different parameters such as the laser power and hatching space were varied to enhance the consolidation of the powder while preventing a significant melting. The influence of the post-SLS heat treatments under air and vacuum on the open pore volume fraction was analyzed. The high-temperature heat treatment under vacuum efficiently reduced the open porosity (despite a high the value close to 31%) and slightly increased the Young's modulus preferentially in one direction (the value ranged from 2 to 12 GPa in the most favorable direction). This study demonstrated the importance of the powder bed step, which significantly influenced the quality of the SLS green body, and thus the properties of the final products after the post-SLS treatments.

References

[1] L.B. Kong, Y. Huang, W. Que, T. Zhang, S. Li, J. Zhang, Z. Dong, D. Tang, Transparent Ceramic, Topics in Mining, Metallurgy and Materials Engineering, Springer, 2015.

[2] P. Hogan, T. Stefanik, C. Willingham, R. Gentilman, Transparent Yttria for IR Windows and Domes – Past and Present, (1) Initial Development of Transparent Yttrium Oxide, 10th DoD Electromagnetic Windows Symposium, 2004.

[3] S.F. Wang, J. Zhang, D.W. Luo, F. Gu, D.Y. Tang, Z.L. Dong, G.E.B. Tan, W.X. Que, T.S. Zhang, S. Li, L.B. Kong, "Transparent ceramics: processing, materials and applications", Progress in Solid-State Chemistry, 41 (2013) 20–54.

[4] M. Mori T. Abe, H. Itoh, O. Yamamoto, Cubic-stabilized zirconia and alumina composites as electrolytes in planar type solid oxide fuel cells, Solid State Ionics, 74 (1994) 157-164.

[5] E. Caproni, F.M.S. Carvalho, R. Muccillo, Development of zirconia–magnesia/ zirconia–yttria composite solid electrolytes, Solid State Ionics, 179 (2008) 1652–1654.

[6] X.J. Chen, K.A. Khor, S.H. Chan, Influence of microstructure on the ionic conductivity of yttria-stabilized zirconia electrolyte, Journal of Materials Science and Engineering. A, 335 (2002) 246–252.

[7] Yuan Ji, Jiang Liu, Zhe Lu, Xin Zhao, Tianmin He, Wenhui Su, Study on the properties of Al_2O_3-doped $(ZrO_2)_{0.92}(Y_2O_3)_{0.08}$ electrolyte, Solid State Ionics, 126 (1999) 277–283

[8] J.F. Baumard, H. Vesteghem, G. Gasgnier, M. Boncoeur, M. Bougoin, “Densification of yttria ceramics”, Advanced Materials Research, 1–2 (1994) 47–54.

[9] H. Zhang, B.-N. Kim, K. Morita, H. Yoshida, K. Hiraga, Y. Sakka, “Fabrication of transparent yttria by high-pressure spark plasma sintering”, Journal of the American Ceramic Society, 94 (2011) 3206–3210.

[10] L. Zhang, J. Feng, W. Pan, “Vacuum sintering of transparent Cr:Y_2O_3 ceramics”, Ceramics International, 41 (2015) 8755–8760.

[11] R. Marder, R. Chaim, G. Chevallier, C. Estournes, “Densification and polymorphic transition of multiphase Y_2O_3 nanoparticles during spark plasma sintering”, Materials Science and Engineering A, 528 (2011) 7200–7206.

[12] M. Ghaderi, R. Shoja Razavi, M.R. Loghman-Estarki, S. Ghorbani, “Spark plasma sintering of transparent Y_2O_3 ceramic using hydrothermal synthesized nanopowders”, Ceramics International, 42 (2016) 14403–14410.

[13] R. Chaim, A. Shlayer, C. Estournes, “Densification of nanocrystalline Y_2O_3 ceramic powder by spark plasma sintering”, Journal of the European Ceramic Society, 29 (2009) 91–98.

[14] H. Yoshida, K. Morita, B.-N. Kim, K. Hiraga, M. Kodo, K. Soga, T. Yamamoto, “Densification of nanocrystalline yttria by low temperature spark plasma sintering”, Journal of the American Ceramic Society, 91 (2008) 1707–1710.

[15] M. Ahsanzadeh-Vadeqania, R. Shoja Razavia, M. Barekata, G. Hossein Borhania, A. Kumar Mishra, “Preparation of yttria nanopowders for use in transparent ceramics by dry ball-milling technique”, Journal of the European Ceramic Society, 37 (2017) 2169–2177.

[16] L. Gan, Y.-J. Park, H. Kim, J.-M. Kim, J.-W. Ko, J.-W. Lee, “The effects of the temperature and pressure on ZrO_2-doped transparent yttria ceramics fabricated by a hot-pressing method”, Optical Materials, 71 (2017) 109–116.

[17] L. Gan, Y.-J. Park, L.-L. Zhu, S.-I. Go, H. Kim, J.-M. Kim, J.-W. Ko, “Fabrication and properties of La_2O_3-doped transparent yttria ceramics by hot-pressing sintering”, Journal of Alloys and Compounds, 695 (2017) 2142–2148.

[18] N. Takata, H. Kodaira, A. Suzuki, M. Kobashi, “Size dependence of microstructure of $AlSi_{10}Mg$ alloy fabricated by selective laser melting”, Materials Characterization, 143 (2018) 18–26.

[19] P. Fathi, M. Mohammadi, X. Duan, A.M. Nasiri, “A comparative study on corrosion and microstructure of direct metal laser sintered AlSi10Mg_200C and die cast A360.1 aluminum”, Journal of Materials Processing Technology, 259 (2018) 1–14.

[20] D. Drummer, S. Greiner, M. Zhao, K. Wudy, “A novel approach for understanding laser sintering of polymers”, Additive Manufacturing, 27 (2019) 379–388.

[21] S. Sing, W. Yeong, F. Wiria, B. Tay, Z. Zhao, L. Zhao, Z. Tian, S. Yang, “Direct selective laser sintering and melting of ceramics: a review”, Rapid Prototyping Journal, 23 (2017) 611-623.

[22] F. Klocke, H. Wirtz, “Selective laser sintering of zirconium silicate”, Proceedings SFF Symposia, (1998) 605–610.

[23] S. Faure, “Etude de l'interaction rayonnement-matière dans un milieu granulaire en vue de l'application au procédé de frittage laser”, PhD Thesis, University of Limoges, 2004.

[24] Y. Zou, C.-H. Li, J.-A. Liu, J.-M. Wu, L. Hu, R.-F. Gui, Y.-S. Shi, “Towards fabrication of high-performance Al_2O_3 ceramics by indirect selective laser sintering based on particle packing optimization”, Ceramics International, 45 (2019) 12654–12662.

[25] P. Bertrand, F. Bayle, C. Combe, P. Goeuriot, I. Smurov, “Ceramic components manufacturing by selective laser sintering”, Applied Surface Science, 254 (4) (2007) 989–992.

[26] Y. Tang, J.Y.H. Fuh, H.T. Loh, Y.S. Wong, L. Lu, “Direct laser sintering of a silica sand”, Materials and Design, 24 (8) (2003) 623–629.

[27] E. Juste, F. Petit, V. Lardot, F. Cambier, “Shaping of ceramic parts by selective laser melting of powder bed”, Journal of Materials Research, 29 (2014) 2086–2094.

[28] I. Shishkovsky, I. Yadroitsev, P. Bertrand, I. Smurov, “Alumina–zirconium ceramics synthesis by selective laser sintering/melting”, Applied Surface Science, 254 (2007) 966–970.

[29] J. Deckers, S. Meyers, J.P. Kruth, J. Vleugels, “Direct selective laser sintering/melting of high density alumina powder layers at elevated temperatures”, Physics Procedia, 56 (2014) 117–124.

[30] A. Danezan, G. Delaizir, N. Tessier-Doyen, G. Gasgnier, J.M. Gaillard, P. Duport, B. Nait-Ali, “Selective laser sintering of porcelain”, Journal of the European Ceramic Society, 38 (2018) 769–775.

[31] A. Sudarev, V. Konakov, Y. Chivel, “Selective laser sintering of ceramic turbomachine components”, Procedia CIRP, 74 (2018) 264–267.

[32] M.X. Gan, C.H. Wong, “Experimental studies on the properties of selectively laser melted alumina–spodumene composite”, Ceramics International, 44 (2018) 19008–19015.

[33] M.X. Gan, C.H. Wong, “Properties of selective laser melted spodumene glass–ceramic”, Journal of the European Ceramic Society, 37 (2017) 4147–4154.

[34] L. Ferrage, G. Bertrand, P. Lenormand, “Dense yttria-stabilized zirconia obtained by direct selective laser sintering”, Additive Manufacturing, 21 (2018) 472–478.

[35] F. Chen, J.-M. Wu, H.-Q. Wu, Y. Chen, C.-H. Li, Y.-S. Shi, “Microstructure and mechanical properties of 3Y-TZP dental ceramics fabricated by selective laser sintering combined with cold isostatic pressing”, International Journal of Lightweight Materials and Manufacture, 1 (2018) 239–245.

[36] Z.H. Liu, J.J. Nolte, J.I. Packard, G. Hilmas, F. Dogan, M.C. Leu, ”Selective laser sintering of high density alumina ceramic parts”, Proceedings of the 35th International MATADOR Conference, (2007) 351–354.

[37] H.H. Tang, M.L. Chiu, H.C. Yen, “Slurry-based selective laser sintering of polymer-coated ceramic powders to fabricate high strength alumina parts”, Journal of the European Ceramic Society, 31 (2011) 1383–1388.

[38] G. Zhang, H. Chena, H. Zhou, “Additive manufacturing of green ceramic by selective laser gasifying of frozen slurry”, Journal of the European Ceramic Society, 37 (2017) 2679–2684.

[39] S. S Liu, M. Li, J. M. Wu, A. N. Chen, Y. S. Shi, C. H. Li, “Preparation of high-porosity Al_2O_3 ceramic foams via selective laser sintering of Al_2O_3 poly-hollow microspheres”, Ceramics International, 46 (2020) 4240-4247.

[40] A.N. Chen, M. Li, J. Xu, C.H. Lou, J.M. Wu, L.J. Cheng, Y.S. Shi, C.H. Li, “High porosity mullite ceramic foams prepared by selective laser sintering using fly ash hollow

spheres as raw materials", Journal of the European Ceramic Society, 38 (2018) 4553–4559.

[41] B. Qian, Z. Shen, "Laser sintering of ceramics", Journal of Asian Ceramic Societies, 1 (2013) 315–321.

[42] G. Lumay, F. Boschini, K. Traina, S. Bontempi, J.-C. Remy, R. Cloots and N. Vandewalle, "Measuring the owing properties of powders and grains", Powder Technology, 224 (2012) 19.

[43] A. Rescaglio, J. Schockmel, N. Vandewalle, G. Lumay, "Combined effect of moisture and electrostatic charges on powder flow", EPJ Web Conf, 140 (2017) 13009.

[44] K. Traina, R. Cloots, S. Bontempi, G. Lumay, N. Vandewalle, F. Boschini, "Flow abilities of powders and granular materials evidenced from dynamical tap density measurement", Powder Technology, 235, (2013) 842–852.

[45] Y.B.P. Kwan, J.R. Alcock, "The impact of water impregnation method on the accuracy of open porosity measurements", Journal of Materials Science, 37 (2002) 2557–2561.

[46] D. Sofia, R. Chirone, P. Lettieri, D. Barletta, M. Poletto, "Selective laser sintering of ceramic powders with bimodal particle size distribution", Chemical Engineering Research and Design, 136 (2018) 536–547.

[47] D. Sofia, D. Barletta, M. Poletto, "Laser sintering process of ceramic powders: the effect of particle size on the mechanical properties of sintered layers", Additive Manufacturing, 23 (2018) 215–224.

[48] S. Dadbakhash, L. Verbelen, T. Vandeputte, D. Strobbe, P. Van Puyvelde, J.P. Kruth, "Effect of powder size and shape on the SLS processability and mechanical properties of a TPU elastomer", Physics Procedia, 83 (2016) 971–980.

[49] A. Dupont, A. Largeteau, C. Parent, B. Le Garrec, J.-M. Heintz, “Influence of the yttria powder morphology on its densification ability”, Journal of the European Ceramic Society, 25 (2005) 2097–2103.

[50] R.L. Carr, “Evaluating Flow Properties of Solids”, Chemical Engineering, 72 (1965) 163–168.

[51] P.A. Cundall, O.D.L. Strack, “A discrete numerical model for granular assemblies”, Geotechnique, 29 (1979) 47–65.

[52] G.V.D. Bergen, “A fast and robust GJK implementation for collision detection of convex objects”, Journal of Graphics Tools, 4 (1999) 7–25.

[53] G.V.D. Bergen, “Efficient collision detection of complex deformable models using AABB trees”, Journal of Graphics Tools, 2 (1997) 1–13.

[54] A. Pilipović, B. Valentan, T. Brajlih, T. Haramina, J. Balic, J. Kodvanj, M. Sercer, I. Drstvensek, “Influence of Laser Sintering Parameters on Mechanical Properties of Polymer Product”, International Conference on Additive Technologies, 2010.

[55] F. Jollet, C. Noguera, M. Gautier, N. Thromat, J.-P. Duraud, “Influence of oxygen vacancies on the electronic structure of yttrium oxide”, Journal of the American Ceramic Society, 74 (1991) 358–364.

[56] Y. Pengfei, Z. Kan, H. Hao, W. Mao, L. Quan, Z. Wei, H. Chaoquan, Z. Weitao, “Oxygen vacancies dependent phase transition of Y_2O_3 films”, Applied Surface Science, 410 (2017) 470–478.

[57] P. Zhang, A. Navrotsky, B. Guo, I. Kennedy, A.N. Clark, C. Lesher, Q. Liu, “Energetics of cubic and monoclinic yttrium oxide polymorphs: phase transitions, surface enthalpies, and stability at the nanoscale”, Journal of Physical Chemistry C, 112 (2008) 932–938.

[58] N. Tessier-Doyen, J.-C. Glandus, M. Huger, "Experimental and numerical study of elastic behaviour of heterogeneous model materials with spherical inclusions", Journal of Materials Science, 42 (2007) 5826-5834

[59] O. Yeheskel, O. Tevet, "Elastic moduli of transparent yttria", Journal of the American Ceramic Society, 82 (1) (1999) 136-144.